

RESEARCH ARTICLE | SEPTEMBER 03 2024

Dynamic and quasi-static strength of additively repaired aluminum ^{EP}

Jesse G. Callanan ^{ID} ; Daniel T. Martinez ^{ID} ; Sara Ricci ^{ID} ; Nicholas K. Brewer ^{ID} ; Benjamin K. Derby ^{ID} ; Brandon J. Lovato ^{ID} ; Kendall J. Hollis ^{ID} ; Saryu J. Fensin ^{ID} ; David R. Jones [✉] ^{ID}

 Check for updates

J. Appl. Phys. 136, 095902 (2024)


<https://doi.org/10.1063/5.0222267>





View Online





Export Citation

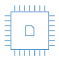
 Nanotechnology & Materials Science

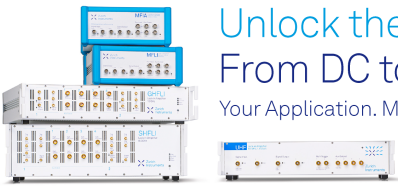
 Optics & Photonics

 Impedance Analysis

 Scanning Probe Microscopy

 Sensors


 Failure Analysis & Semiconductors



Unlock the Full Spectrum. From DC to 8.5 GHz.

Your Application. Measured.

[Find out more](#)



Dynamic and quasi-static strength of additively repaired aluminum

Cite as: J. Appl. Phys. **136**, 095902 (2024); doi: [10.1063/5.0222267](https://doi.org/10.1063/5.0222267)

Submitted: 6 June 2024 · Accepted: 12 August 2024 ·

Published Online: 3 September 2024



Jesse G. Callanan,¹  Daniel T. Martinez,¹  Sara Ricci,^{1,2}  Nicholas K. Brewer,¹  Benjamin K. Derby,¹ 
Brandon J. Lovato,¹  Kendall J. Hollis,³  Saryu J. Fensin,¹  and David R. Jones^{1,a)} 

AFFILIATIONS

¹Materials Physics and Applications Division, Center for Integrated Nanotechnologies, Los Alamos National Laboratory, Los Alamos, New Mexico 87545, USA

²DICEM, University of Cassino and Southern Lazio, Cassino, IT-03043, Italy

³SIGMA Division, Fabrication Manufacturing Sciences, Los Alamos National Laboratory, Los Alamos, New Mexico 87545, USA

^{a)}Author to whom correspondence should be addressed: djones@lanl.gov

ABSTRACT

Additive manufacturing has the potential to repair high value components, saving significant time and resources; however, the level of reliability and performance of additive repairs is still relatively unknown. In this work, the structure–property and performance of laser wire additive manufacturing repairs in 1100 aluminum are investigated. Two types of intentional damage are inflicted on the samples and subsequently repaired with pulsed laser deposition additive manufacturing. Quasi-static (10^{-3} s^{-1}) and high strain-rate (10^{-3} s^{-1}) mechanical testing is carried out with *in situ* diagnostics and post-mortem imaging. The results show that while the quasi-static strength and ductility of samples with a repaired region are lower than a pristine sample, the dynamic strength under shock loading is comparable. This work highlights both the potential utility of additive manufacturing for repair purposes, the significant risk of compromised performance of additive parts under specific conditions, and the need to test at varying strain rates to fully characterize material performance.

© 2024 Author(s). All article content, except where otherwise noted, is licensed under a Creative Commons Attribution-NonCommercial-NoDerivs 4.0 International (CC BY-NC-ND) license (<https://creativecommons.org/licenses/by-nc-nd/4.0/>). <https://doi.org/10.1063/5.0222267>

I. INTRODUCTION

Aluminum and its alloys are some of the most widely used engineering materials in aerospace, defense, automotive, and construction applications. Aluminum alloys offer a high strength to weight ratio at a reasonable cost and are widely available. However, compared to other engineering materials such as steel or titanium, aluminum is relatively soft and, therefore, susceptible to damage from small impacts, such as scratches, dents, and dings. In circumstances where a scratch or dent leads to a millimeter-scale damage site, the entire component may be compromised, which forces time-intensive and costly replacements.

Additive manufacturing (AM) has the potential to greatly reduce the time and cost associated with restoring damaged components. AM has several highly desirable advantages in terms of repair, namely, small localized heat input, material versatility, geometric and structural versatility, and increasing accessibility and reliability. Aluminum alloys are widely used in many AM processes,^{1–4} and

material properties, microstructure, and density, and overall performance are continuously improving.^{5–10} The relationship between the material processing, structure, properties, and performance is crucial to understand for component reliability, optimization, and use in any applications. The unique thermal process history that AM parts experience along with other environmental, chemical, feedstock, and geometry (i.e., mechanical stress during build) effects often lead to unpredictable or undesirable microstructure which in turn leads to compromised properties and performance or, in the best case, unexpected performance attributes (high ultimate strength with low ductility, for example). Before AM can be widely used to make repairs on parts that will be in service, the performance must be predictable and the relationship between the AM process and the material characteristics must be understood.

One key performance metric is tensile strength. Tensile strength is a strain-rate dependent material property, and for use in aerospace or defense applications, a wide range of strain-rates (10^{-3} – 10^6 s^{-1}) must be considered—often, the most dramatic and catastrophic

09 September 2024 08:20:42

failure modes of a component occur under high strain-rate (i.e. blast, impact, or ballistic) loading. Tensile strength at a high strain-rate is often understood in terms of the material spall strength, which indicates the internal tensile load, which causes severe damage nucleation at high strain-rate.^{11,12}

In this work, 1100-series aluminum samples were prepared with intentional small damage sites (indents or scratches), which would predictably compromise the performance.¹² The indents or scratches were repaired with laser wire-fed additive manufacturing using 1100 filler wires. The repairs were characterized along with the as-received undamaged material; while the laser AM repairs showed some flaws, namely, a few isolated large ($10\ \mu\text{m}$ radius) pores in each sample, overall, the density was close to 100%. Both quasi-static tensile dogbones and dynamic shock loading targets were prepared with scratches, and shock loading targets were also prepared with circular indent damage sites. The repaired samples were tested, and the performance of the repair was evaluated relative to the pristine sample. The results show that at a very low strain-rate, the repair is ineffective and the part fails at a much lower stress and exhibits much less elongation. At a high strain-rate, however, the repair region is nearly invisible to the shock wave and the spall strength is comparable to that of the pristine case.

II. SAMPLE PREPARATION

A. As-received material

The microstructure of the pristine 1100 aluminum is shown in Fig. 1. The scanning electron microscopy (SEM) images and the

electron backscatter diffraction (EBSD) image show the crystal structure and the presence of some inclusions in the as-received material. The grains are textured along the rolling direction and there is evidence of a high number of inclusions in the micrograph. The 1100 aluminum plates were machined into three types of samples: pucks, which would be used to examine the pristine and repaired material without loading, dogbones, which would be used in quasi-static testing, and cylindrical targets, which would be subjected to shock loading. The cylindrical pucks are differentiated from the targets to clarify which samples were shocked, but the geometry is the same.

B. Intentional damage procedure

To test the effectiveness of the laser AM repair procedure, the samples were intentionally damaged on one face. Two damage types were implemented: scratches, which remove material in sequential small-depth passes with a sharp cutting tool, and indents, which displace material and severely deform the microstructure via impact with a weighted conical indenting bit. An example of the indent damage site is shown in Figs. 1(d)–1(f), and an example of the scratch damage type is shown in Fig. 3(c). The scratches varied from 250 to $1000\ \mu\text{m}$ in depth, and the cutting tool was a 60° triangle with a $0.2\ \text{mm}$ tip radius and 7° relief angle. The indents were made with a steel center locating punch insert, which had a 45° cone of diameter $2\ \text{mm}$, which leads into a hexagon of inscribed diameter $2\ \text{mm}$ and was threaded directly into a force transducer in a small drop tower. In the future, a different

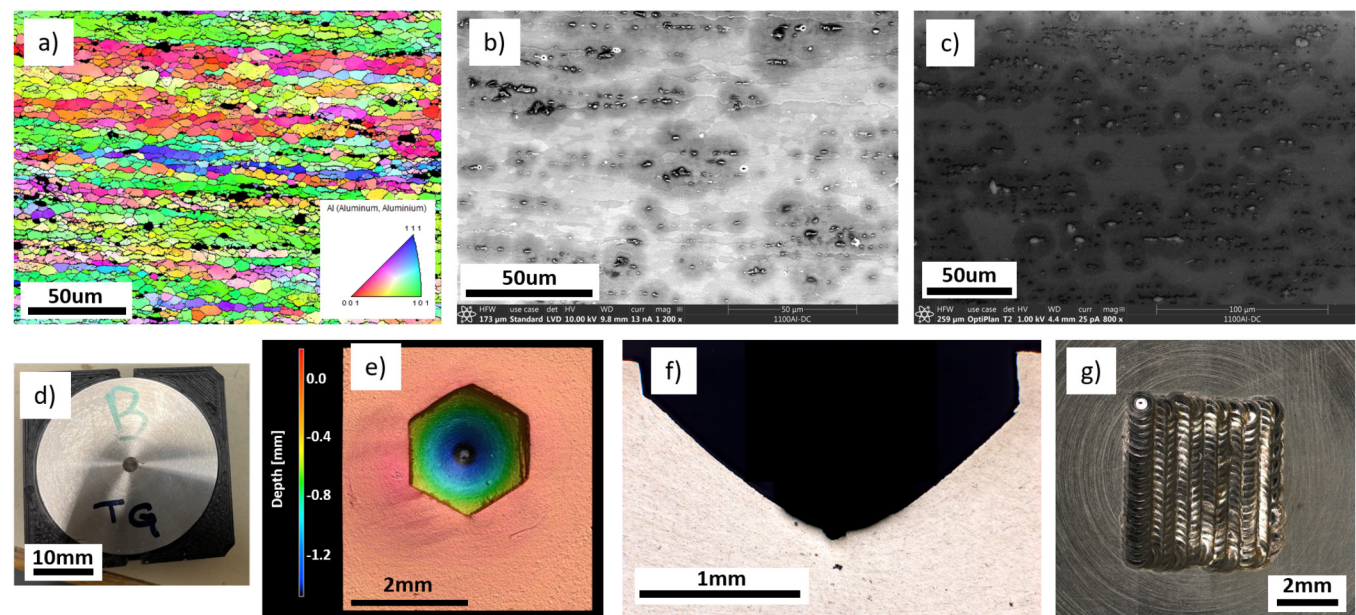


FIG. 1. Pristine as-received 1100 aluminum micrographs obtained using (a) electron backscatter diffraction, (b) low vacuum detector scanning electron microscopy, and (c) secondary electrons in the scanning electron microscope. The strong texture from plate rolling is evident in (a), and some inclusions or elemental segregation are evident in (b) and (c). An example of an intentional indent site in a shock loading target is shown in (d) with a laser confocal microscopy image in (e), optical microscopy of an indent cross section in (f), and an additive weld repair shown in (g).

material should be used for the conical indenter inserts since steel leads to some contamination, which was present through the repair process. An example of an indented target before shock loading is shown in Fig. 1(d). Laser confocal microscopy imaging of a different unshocked indent is shown in Fig. 1(e) to quantify the depth and geometry. The indented sample was sectioned and polished, and the optical microscopy image in Fig. 1(f) shows both the indent geometry and the microstructure deformation.

C. Additive manufacturing repair

The additive repairs were performed with a Sunstone Welders Orion LZR 160 laser welder and a custom built five axis motion platform. The LZR welder had a 1064 nm Nd:YAG laser with 8 kW peak power and 160 J output. The laser focal point was fixed in space, and the motion platform was used to move the sample to melt different regions or add filler material. The motion platform consisted of three Thorlabs MTS25-Z8 motorized translation stages, which provided three translational degrees of freedom. The system was also equipped with two DDR25 compact drive rotation mounts, one of which drove a worm gear to control the pitch while the other held the sample with a vice and controlled the rotation (yaw). All the stages were operated with Thorlabs Kinesis software, which allowed for a constant speed of translation and/or rotation. A rectangular raster pattern was used for each repair as shown in Fig. 1(g). The system is described in detail in previously published works.¹²

The repairs used 1100 aluminum wires with a circular cross section of diameter 0.5 mm. The laser was set to 4 kW with 3 ms pulse time, 0.8 mm spot size, and a pulse rate of 2 Hz. At each layer, a full area coverage of autogenous welds was carried out to melt the previous layer. After the remelting, filler material was added in small amounts until the area was covered with the filler wire, and then another series of autogenous welds were conducted. The repair was made proud over the top surface of the original cylinder and then ground back and lapped flat to the original sample dimension after it was complete. Due to chemical contamination, several repairs were porous. The as-repaired microstructure is shown in Fig. 2. The main figure, Fig. 2(a), shows a stitched image of a full puck with a scratch that was repaired. The detail callout makes the original pristine microstructure visible via the rolling texture and inclusions in contrast to the more uniform colored repair region. A large pore is visible within the repair and the melt pool lines are faintly apparent. An EBSD map is overlaid on the detail callout and shown in full in Fig. 2(b). In the EBSD map, the original microstructure is visible in the lower half and lower right corner with strong horizontal texture and some inclusions, which appear as small black regions. The repair area, in the top and upper left corners, is visible with characteristically large columnar grains and melt pool lines, which appear from the superimposed image quality grayscale.

The intentional indent damage process may have introduced steel oxides into the surface of the repair site. It is likely that the indenter forcefully lodged steel and black oxide coating particles into the surface of the aluminum during the indenting process.

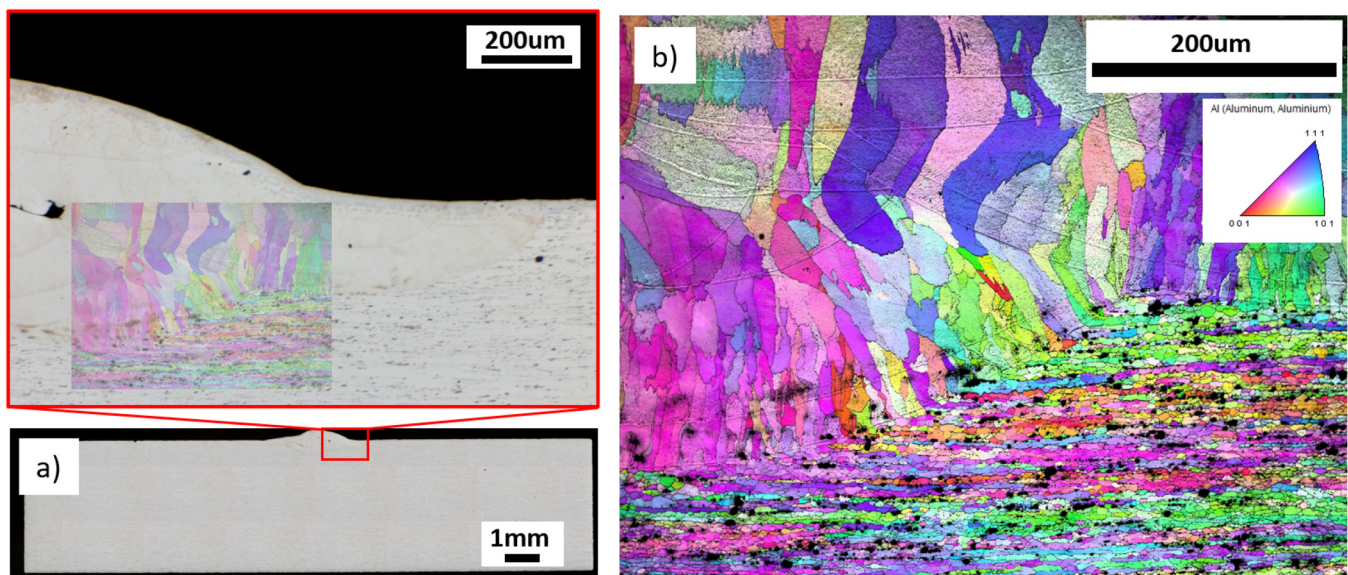


FIG. 2. Repaired scratch puck sample showing (a) optical micrograph stitch with the zoom region, which highlights the pristine/original material microstructure at the bottom and AM weld repair at the top. The weld was built proud of the top surface of the sample, and a single large pore is visible in the bulk of the repair region. The transparent overlay corresponds to the electron backscatter diffraction map in (b) which clearly shows the original, textured microstructure of the rolled plate from which the sample was cut, in contrast to the large columnar grains of the repair region. The AM weld melt pools can be made out due to the image quality grayscale that is shown along with the inverse pole figure colormap. The build direction is toward the top of the page.

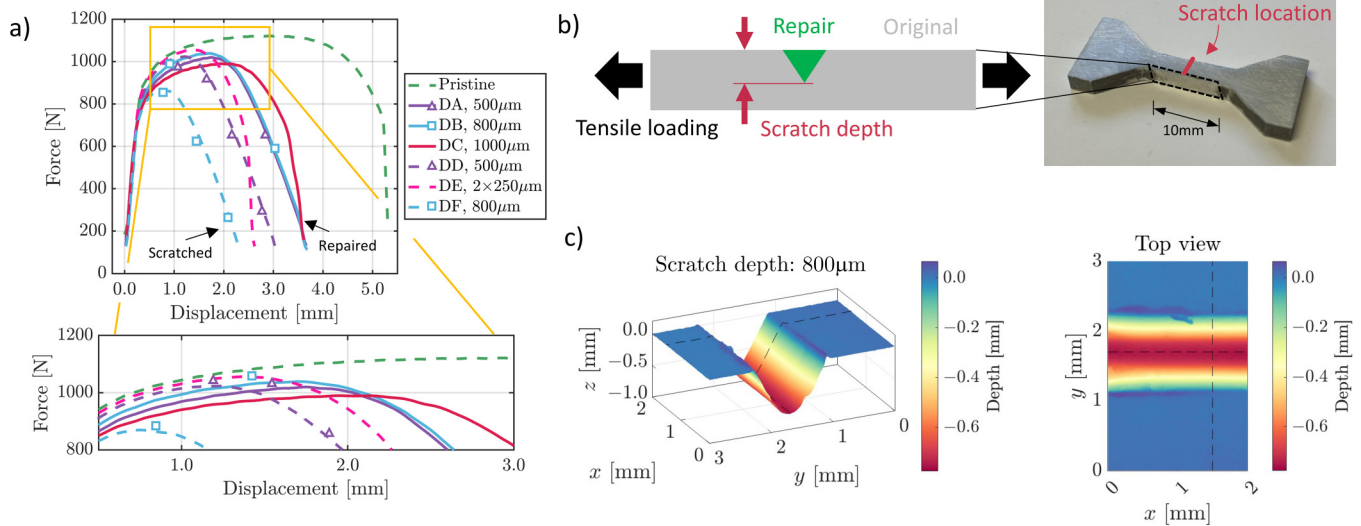


FIG. 3. Quasi-static AM repair testing results: (a) tensile test force–displacement curves showing the pristine sample and three different scratch/repair depths, (b) tensile dogbone sample photo and repair geometry and location illustration, and (c) laser confocal microscopy profile of a scratched sample in isometric and top-down view showing the scratch geometry before repair. Sample DE had two scratches of depth 250 μm placed on either side of the sample to determine the influence of the scratch asymmetry with no repair: the effective reduction in cross-sectional area is the same as DD but the scratches are symmetric across the sample.

This led to significant contamination during the repair and was a probable source of porosity. The geometry of the porosity in Fig. 2(a) and the callout implies that some organics or chemicals were volatilized during the repair. Further sources of contamination that should be accounted for in future work include oxidation of the filler wire, which due to its large surface area to volume ratio may have introduced a significant amount of oxides into the repair, and oxidation of the aluminum sample surface itself, which was possible despite the use of argon shielding gas.

III. QUASI-STATIC TESTING

The 1100 aluminum dogbone samples, pristine, scratch repaired (dogbone DA with 500 μm deep scratch repair, dogbone DB with 800 μm , and dogbone DC with 1000 μm deep scratch repair), and scratched with no repair (dogbone DD with 500 μm deep scratch, dogbone DE with two 250 μm scratches, one on each side, and dogbone DF with 800 μm deep scratch) were tested at quasi-static strain-rate under uniaxial force loading to determine the tensile strength and failure mode under uniaxial low strain-rate conditions. A total of seven dogbone specimens were tested, and all the force–displacement results are presented in Fig. 3. The quasi-static tests were carried out at 10^{-3} s^{-1} using an MTS hydraulic load frame. A photo of an untested dogbone sample is shown in Fig. 3(b), and the sample was 31.75 mm long with gauge section length 12.7 mm and thickness 3.18 mm. The dogbones were scratched in the middle of the gauge section on one side as shown in Figs. 3(b) and 3(c). The scratch geometry is shown in Fig. 3(c) for an example case of a 800 μm scratch depth. Laser confocal microscopy was used to capture the surface geometry and texture of the sample before the repair was made. The color and

three-dimensional rendering of the sample surface demonstrates the consistency and uniformity of the scratch intentional damage site. After the repair, the AM material was filed back and the sample surface was sanded smooth. The repairs were not visible to the naked eye, but the results shown in Fig. 3(a) demonstrate that the tensile strength of the samples was compromised significantly compared to the pristine case. The results in Fig. 3(a) are left in terms of force and displacement as measured directly during testing. Since the sample cross section is not uniform (i.e., the weld is only on one side), the stress is not uniaxial. For the pristine case, the uniaxial conditions do apply, so the stress and strain are reported in Sec. III A for that case. In future work, it may be possible to develop a repair specimen geometry that has a uniform cross section at each point along the gauge length (to achieve the uniaxial condition in a repaired sample) by cutting the sample completely and including a fully repair material region, but that is beyond the scope of this work due to limitations in the AM system.

A. Quasi-static behavior

The quasi-static yield stress and ductility of the repaired samples were significantly lower than the pristine case. The pristine sample had an ultimate tensile strength of 137 MPa and a max strain of 0.35. While the ultimate strength could not be accurately determined for the repaired samples due to the non-uniform stress distribution, examining Fig. 3(a) shows that both the yield and strain to failure are significantly lower for all three repair depths. In Fig. 3(a), the repaired samples are shown in solid lines and the samples with no repair—including the pristine sample—are shown in a dashed line. The markers indicate which samples are comparable between the repair and un-repaired cases, i.e., the solid line

with a triangular marker is sample DA with a repaired $500\ \mu\text{m}$ scratch, and the dashed line with the triangular marker is sample DD with the un-repaired $500\ \mu\text{m}$ scratch. The elastic response of all seven samples is qualitatively the same; however, there are differences in yield force where the material transitions to plastic deformation. Specifically, there is a decrease in the yield force as a function of increasing defect size, with the $1000\ \mu\text{m}$ deep scratch repair approximately $100\ \text{N}$ below the pristine case, and the un-repaired $1000\ \mu\text{m}$ more than $200\ \text{N}$ lower. The repaired samples DA and DB can be directly compared to their un-repaired counterparts DD and DF. The comparison shows that while the repair did not fully recover the strength of the pristine sample, it did improve the strength relative to the un-repaired cases. Interestingly, sample DB showed a slightly higher ultimate force than case DA even though the repair region was larger. It is possible that the repair has a higher ultimate strength than the original material but the repair interface likely has a lower strength than both materials. Since case DC had a very large repair interface, it failed quickly. It is possible that case DB benefited from the higher strength of the repair material relative to case DA without being compromised by the repair interface to the same extent as case DC. Further testing would be necessary to confirm this quantitatively.

B. Digital image correlation

During tensile testing, digital image correlation (DIC) was used to track the deformation of the sample. The pristine samples showed uniform deformation under the uniaxial load as expected; the failure was symmetric and the necking was the same on all sides. The repaired samples, however, have a degree of asymmetry in their material properties due to the triangular prism-shaped repair region, which has a substantially different microstructure. This asymmetry in material structures leads to a difference in performance along the cross section of the dogbone. This asymmetry in strength was captured by the DIC process. The samples were prepared with speckled paint, and video recordings were synchronized with the load frame operation. The videos were post-processed and analyzed to track the individual speckles on the sample. Tracking the speckles allowed for a map to be constructed which can show strain, position, velocity, or other positional parameters. The results are shown in Fig. 4 along with an illustration depicting the camera view direction, which shows it is looking parallel to the scratch direction.

Two frames from the DIC recording series are shown on the left side of Fig. 4: the undeformed sample before testing, and the sample just at failure. The speckled paint is visible and in the lower photo of the sample at failure, the asymmetry can be observed. A callout illustration explains the failure mode: the repair region appeared to separate from the base material at the interface. The colorful DIC image contour map in Fig. 4 shows the displacement of each pixel on the sample just at failure, and with an illustration of the triangular repair region overlaid in gray. The colormap shows that the sample deformation is asymmetric: the material on the left side of the sample, the base material from the original 1100 plate which is “under” the repair, deformed substantially and showed characteristic necking similar to what was observed in the pristine case. The right side of the sample, however, showed very

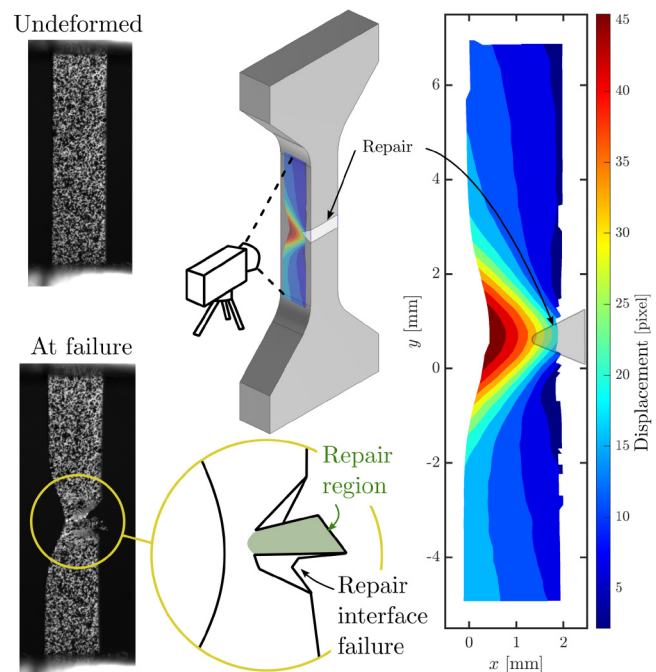


FIG. 4. Digital image correlation analysis of scratch repaired 1100 aluminum sample dogbone DA ($500\ \mu\text{m}$ scratch depth with repair) under quasi-static loading. The colormap shows the displacement from the original, unloaded position of each location on the sample. The displacement is highly asymmetric, indicating that the necking behavior is non-uniform: the original material deforms significantly, while the repair region does not deform.

little deformation. The color corresponds to the displacement in terms of pixels: the bright red region, which showed the most deformation is where the original material is. This result indicates that the repair was less ductile than the original material and failure initiated at the repair boundary.

C. Fractography

The post-mortem quasi-static dogbone samples were mounted in a SEM and imaged to determine the failure modes under low strain-rate loading. The SEM images are shown in Fig. 5 for dogbone sample DC. The SEM images show differences in the fracture morphology between the original material and the repair material. In Fig. 5(a), the original material is on the bottom half of the image, and the repair material is in the top half of the image. The pristine material, which is underneath the repair region during the AM process, shows characteristically ductile fracture traits such as dimpling. The repair region, however, appears to show a different failure mode. The large fracture surfaces at the top of Fig. 5(a) appear to correspond to the larger grains in the AM region. They also indicate a more brittle failure mode. The lower ductility of the AM repair region offers some explanation for the reduced strength of the repaired dogbones under quasi-static loading: the original material, with its considerable ductility, does not benefit from the

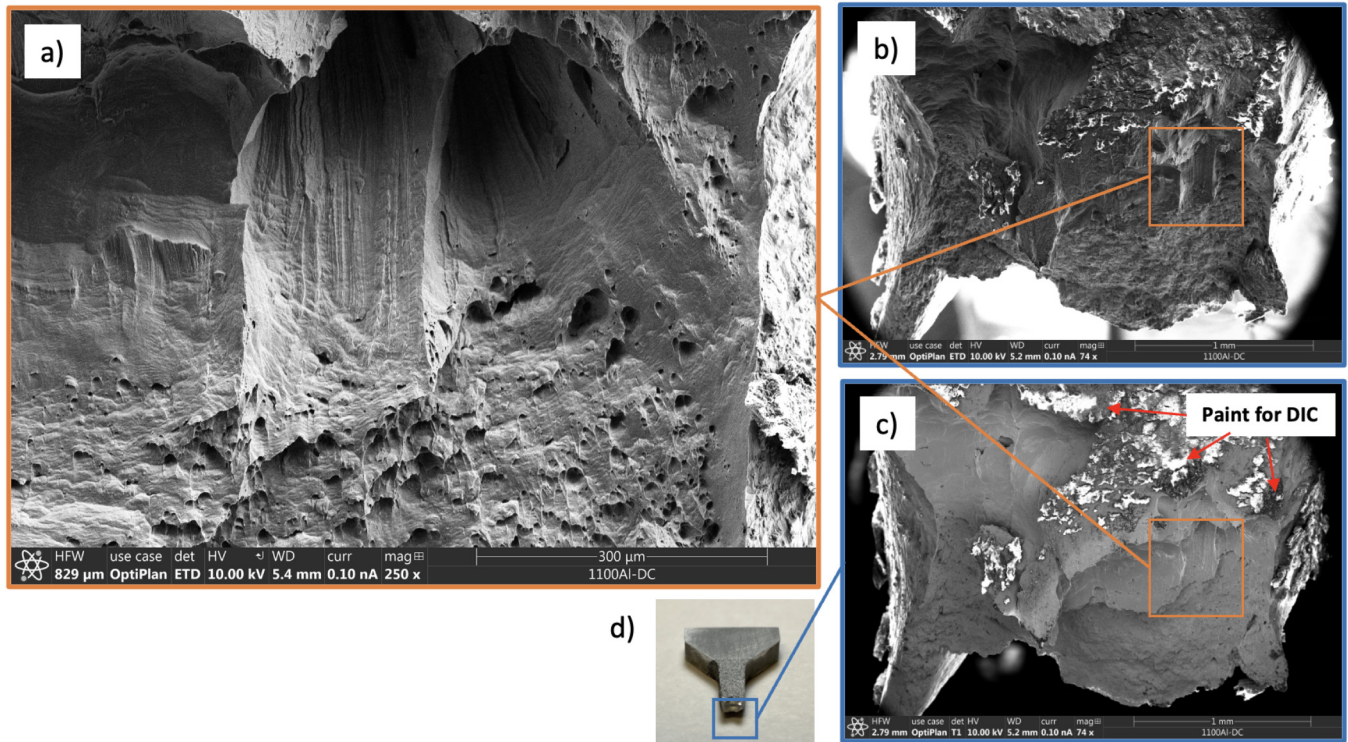


FIG. 5. Scanning electron microscopy of the fracture surface of the dogbone sample DC (1000 μm scratch depth with repair) after quasi-static loading. Detail view (a) shows the closeup of the key fracture surface where the repair region is roughly at the top half of the image and the original material is roughly at the bottom half: the original material shows evidence of highly ductile fracture, while the repair shows more brittle characteristics and large smoother regions. The intermediate zoom views in (b) and (c) show two angles, which both include the zoom view in (a) but also show the context within the entire sample, and the photo in (d) shows the reference location in the entire half of the original dogbone.

repair since the repair behaves in a more brittle manner. This result agrees with the published literature on additively manufacturing aluminum which showed brittle failure and very low fracture elongation.¹³

IV. SHOCK TESTING

The shock impact testing was carried out on a 19 mm bore light-gas gun. Argon gas was pressurized inside of a wrap-around breech, and a dual o-ring projectile made of Lexan and fitted with a flyer plate was launched down the barrel. An illustration of the impact setup is shown in Fig. 6: the projectile with flyer plate (copper in this case) and its velocity direction, the stationary sample with repair or indent location, and laser velocimetry measurement position are all indicated. The back of the flyer plate was fitted with syntactic foam to support the flyer during launch. Projectile velocity immediately before impact was measured with a pair of laser light-gates spaced at a known distance. The sample was secured on the front face of a catch tank and aligned to the barrel axis. The sample was tapered to aid in recovery and fitted with an 1100 aluminum momentum ring such that edge releases were minimized in the spall region. The rear free-surface velocity was measured with up-shifted photon Doppler velocimetry (PDV)

during impact.¹⁴ After impact, the projectile was stopped by the catch tank and the sample was soft captured for further analysis. More details on the experimental setup are available in previously published studies.^{11,15,16} It is important to note for this work that

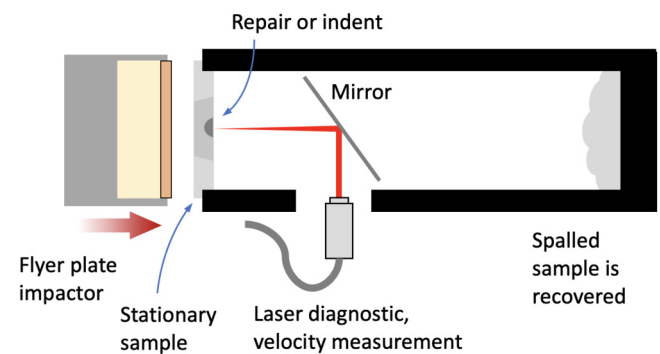


FIG. 6. Illustration of shock loading impact setup: incident projectile with copper flyer plate, stationary sample with repair, indent, or scratch location, laser velocimetry, and post-impact sample recovery setup with catch tank.

09 September 2024 08:20:42

TABLE I. Shock target sample set with sample name (i.e., target TA, target TF, and target TG), impact velocity (v), condition of samples, peak stress (σ_{peak}), and spall strength (σ_{sp}). Note that some quantities are reported as NA (not applicable) in non-equilibrium cases. The uncertainty in the impact velocity measurement, peak stress, and spall strength are 5 m/s, 0.1 GPa, and 0.2 GPa, respectively.

Sample	v (m/s)	Condition	σ_{peak} (GPa)	σ_{sp} (GPa)
TP ₁	226	Pristine (1)	2.36	0.87
TA	251	Indent/repair	2.69	0.95
TF	224	Scratch/repair	2.33	0.85
TG	226	Scratch/repair	2.31	0.81
TD	228	Indent/damage	NA	NA

the PDV was aligned to measure as close to the center of the target as possible, and, thus, in the un-repaired indent cases, the measurement was taken at the bottom of the indent cone. A summary of the quantitative results of the high strain-rate testing is shown in Table I. A total of eight samples were tested between repaired, un-repaired, indents and scratches, but only a subset is presented here. The omitted cases showed either redundant results (the PDV from several indent cases) or very poor repair quality due to contamination in the AM process.

A. In situ velocimetry and spall strength

The laser velocimetry measurements taken during shock loading shows the performance of the repair and can be used to calculate the spall strength of the sample. The peak stress (or Hugoniot state) experienced by the sample during the impact

experiment, σ_{peak} , can be calculated using

$$\sigma_{\text{peak}} = \rho_0 U_s u_p, \quad (1)$$

where U_s is the shock wave speed and u_p is the peak particle velocity. The peak particle velocity is found approximately from the free-surface velocity as $u_p \approx 1/2 u_{fs, \text{peak}}$, and the shock speed can be estimated as $U_s = c_0 + s u_p$, where c_0 is a fitting parameter and s is the Hugoniot slope coefficient.^{17,18} Since the equation of state was not measured in this study, the literature value of $s = 1.34$ was used for the Hugoniot slope parameter and $c_0 = 5.38 \times 10^3 \text{ ms}^{-1}$ was used for the fitting parameter.¹⁸

The difference in the peak velocity in the flat-topped region and the first subsequent minima before the reload of the free surface is used to calculate the spall strength of the material. The spall strength, σ_{sp} , can be computed using

$$\sigma_{\text{sp}} = \frac{1}{2} \rho_0 c_B (\Delta u_{\text{sp}}), \quad (2)$$

where the change in velocity from the flat-topped peak to the valley just before acceleration is the pullback velocity defined as Δu_{sp} . The bulk sound speed c_B is computed from the measured longitudinal and shear sound speed, c_L and c_S , as

$$c_B = \sqrt{c_L^2 - (4/3)c_S^2}. \quad (3)$$

The sound speed of the pristine material was measured with a pulse-echo ultrasonic pulser-receiver, and the density was computed from the mass and volume. The longitudinal sound speed of the pristine sample was measured to be $(6.520 \pm 0.003) \text{ mm}\mu\text{s}^{-1}$,

09 September 2024 08:20:42

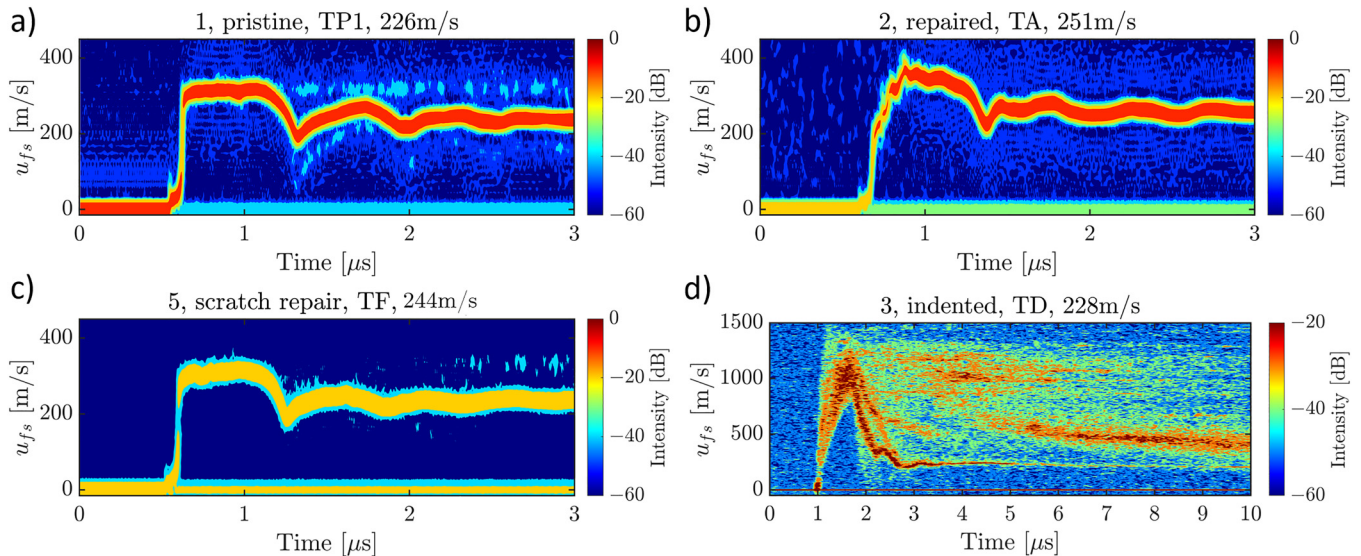


FIG. 7. Photon Doppler velocimetry measurements for shock loading targets: (a) spectrogram of pristine target, (b) spectrogram of repaired indent target, (c) spectrogram of repaired scratch target, and (d) spectrogram of un-repaired indented target which shows extreme velocity overshoot and material ejected off the rear surface.

shear sound speed $(3.130 \pm 0.003)\text{mm}\mu\text{s}^{-1}$, and density $(2.68 \pm 0.02)\text{g cm}^{-3}$.

The *in situ* velocity profiles are shown in Fig. 7. Note that the horizontal and vertical axis scales in Fig. 7(d) are different from the other three graphs: Fig. 7(d) is the un-repaired indent case, TD, and exhibits extremely high maximum velocity and significant streaking, which is evidence of ejected material and possibly jetting. This measurement emphasizes the need for repairing even small scratches or dings in parts that might be subject to shock loading: the free-surface velocity within the indent conical region is three times greater than the peak velocity of the pristine case. This velocity overshoot is attributed to a wave focusing effect, similar to a shaped charge. The spectrogram corresponding to the pristine target is shown in Fig. 7(a): the pristine sample shows the expected change in slope at the Hugoniot elastic limit, a steep shock rise with flat top at peak pressure, and the characteristic pullback with reload at roughly $t = 1.3\mu\text{s}$, which indicates the formation of internal tensile damage. The indent repair case, TA, shows a considerable velocity overshoot with some oscillations at peak velocity and a lack of clean flat-top velocity at peak stress. This indicates that

there was likely some porosity present in the sample¹¹, which is believed to have originated from black oxide steel remnants that were lodged into the surface of the indent. The repair, however, is still highly effective at reducing the dramatic velocity overshoot that was observed in sample TD in Fig. 7(d). Note that the impact velocity for TA is 25ms^{-1} greater than the pristine sample TP1. The next repair case, TF (scratch repair), showed behavior that was much closer to the pristine case with typical elastic-plastic transition, steep shock rise, and nice flat top with a pullback that is almost identical to the pristine case. The scratch damage sites were made using a lathe insert cutting tool which did not leave any contamination and, thus, the repairs were cleaner. In all cases, the AM repair was successful at eliminating the dramatic velocity overshoot and recovering behavior that was similar to the pristine case.

In comparison to the dramatic features observed in Fig. 7(d), even the most porous repair shown in Fig. 7(b) is a significant improvement; the other repair cases performed even better. The similarities in the free-surface velocity response (and damage morphology, as will be discussed later) between the repair and pristine case are determined to be, for the purpose of this work, sufficient to call the repair successful as compared to the indented case. Future work investigating the correlation between the repair properties (i.e., porosity which contributes to bulk density, repair material impedance, process parameters, etc.) and repair performance

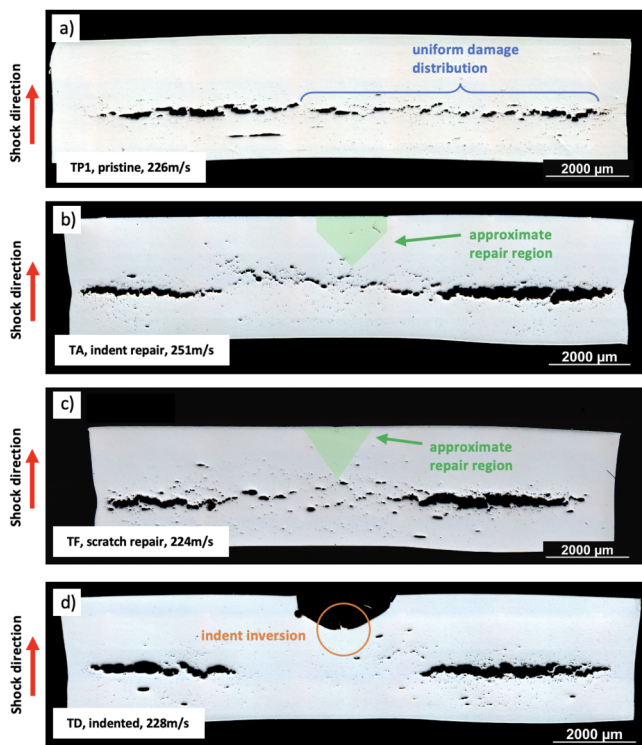


FIG. 8. Post-mortem metallography results for shock loaded spall samples: (a) pristine 1100 aluminum sample with benchmark uniform damage distribution for incipient spallation, (b) AM repaired conical indent with repair region illustrated showing some irregularities in damage distribution, (c) AM repaired scratched sample showing similar damage formation to indent case, and (d) unrepaired indent sample showing no damage formation under indent and inverted geometry at the base of the conical region.

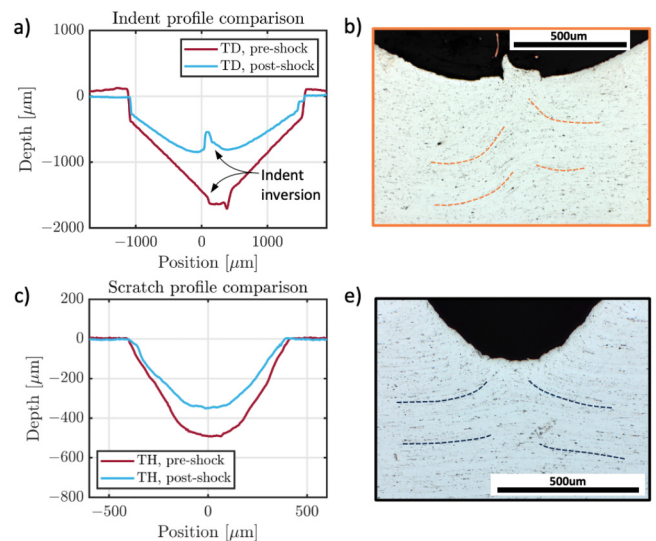


FIG. 9. Change in geometry of indent and scratch: (a) confocal microscopy profile line of pre- and post-shock indent geometry, which clearly shows an inversion of the conical point feature after shock loading, and a definite material spike in the center, which was likely the source of the measured high velocity free-surface features, (b) post-mortem metallography showing the inversion spike as well as the re-directed features, which appear pushed up toward the spike, (c) change in geometry profile for scratch target, which is less dramatic due to the symmetry and smaller wave focusing effect, and (d) post-mortem optical image of scratch microstructure showing the same pushed/pinched effect from the wave focusing. Note that dashed lines have been included to guide the eye along the directions of the inclusion stripe deformations.

09 September 2024 08:20:42

(velocimetry similarities, post-mortem damage, quasi-static, and dynamic strength) is necessary in order to begin to bound the definition of when a repair is successful; that quantitative bounding process is beyond the scope of this work.

B. Post-mortem metallography

The shock loading targets were recovered after impact and sectioned along their diameter. The sections were mounted in epoxy and ground with increasingly fine SiC paper, then polished with $1\mu\text{m}$ alpha alumina slurry and then $0.04\mu\text{m}$ colloidal silica. Optical images of the polished samples are shown in Fig. 8. Figure 8(a) shows the pristine sample, which serves as the performance benchmark. The incipient spall damage is formed approximately at the center of the sample and shows ductile void growth as expected. The additively repaired indented sample, TA, is shown in Fig. 8(b). The approximate region of the AM repair is highlighted. The spall damage distribution is observed to be similar in overall trend as compared to the pristine sample case, but slightly more irregular. The damage is seemingly concentrated in the first and last third of the sample width, and the center third (directly under the repair) is slightly less intense per unit area. The same trend is true for the AM repaired scratch case shown in Fig. 8(c): the damage distribution seems more bi-modal than in the pristine case; however, voids are still observed across the entire width. In the un-repaired indent case, Fig. 8(d), two new features appear: the damage is only present in the first and last third of the sample, and the indent geometry has changed significantly. The lack of damage

in the center third of the indented sample demonstrates a “shadow” effect that occurs when the shock transit time is different due to the change in the geometry—the rarefaction waves do not interact to create a region of high tension, and, therefore, no spall occurs immediately under the indent.

The indent inversion phenomenon is shown in detail in Fig. 9. The line charts in Figs. 9(a) and 9(c) are laser confocal microscopy profiles of the before and after shock loading indent or scratch geometry. Before shock loading, both geometries are as expected, with the indent size in Fig. 9(a) corresponding to the size of the indenter, and the scratch geometry in Fig. 9(c) matching that of the scratch profiles from the quasi-static dogbones as expected. After shock loading, however, the geometry of both cases has changed. The indent shows an inverted tip in what was the center point of the cone, and the overall depth is less. The scratch depth was decreased and the shape was flattened out. Optical micrographs in Figs. 9(b) and 9(d) reveal that the material deformation is directed into the indent or scratch: where before shock loading, the grains were either textured horizontally (due to plate rolling of the as-received material as shown in Fig. 1), now the inclusions form stripes that are peaked and pointed upward in the center near the indent. The same trend is observed for both the scratch and conical indent geometry; however, only the indent shows the inversion spike.

A large montage EBSD scan is shown in Fig. 10, sample TA, AM indent repair, after shock loading. The scan shows the original plate material with highly textured grains, as well as the parabolic-shaped deformation that occurred during the indentation damage

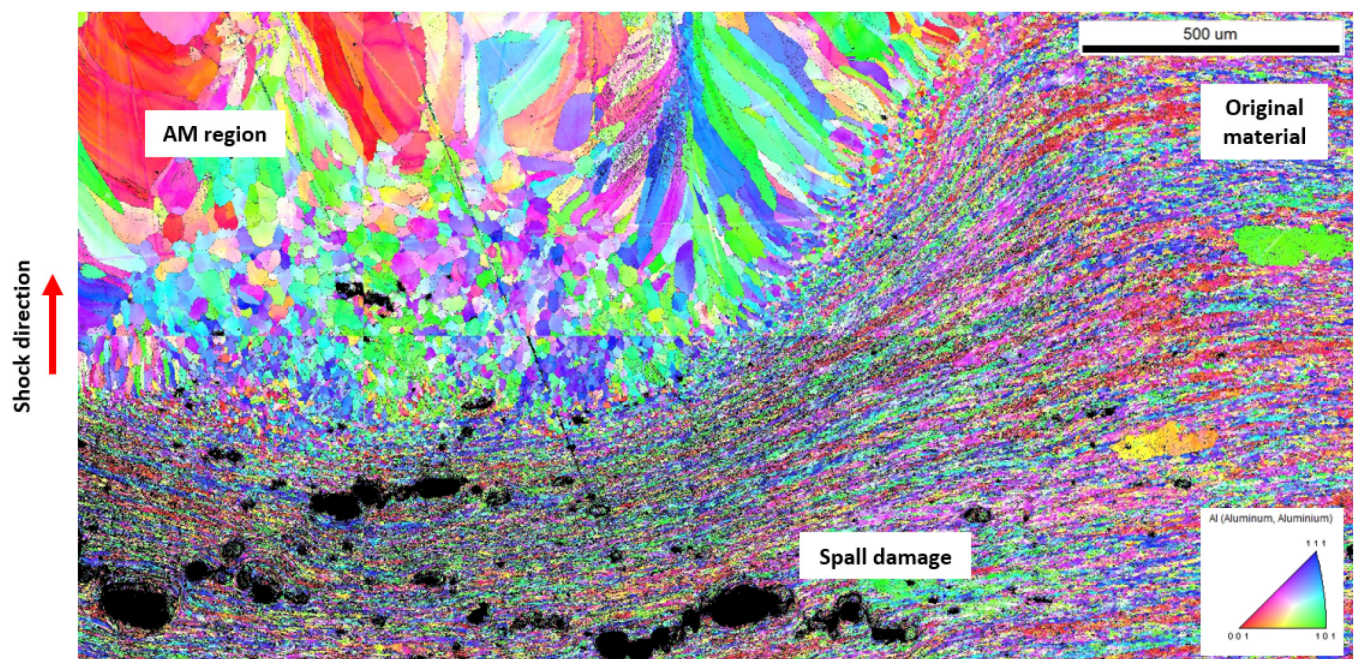


FIG. 10. Post-mortem electron backscatter diffraction image of sample TA, which was intentionally indented, repaired with wire-fed laser additive manufacturing, and then subjected to shock loading to form incipient spall damage at high strain-rate.

process. The AM region can be observed in the upper left region of the image with the large grains and some distinct and familiar evidence of rapid cooling, thermal gradients, and repeated heat cycling. The spall damage appears in the bottom half of the image, predominantly in the pristine material due to the design of the experiment—the sample and flyer thickness were chosen such that the spall plane occurred in the middle of the sample, but the repair does not extend to that depth. This image demonstrates that the repair region does not influence the damage nucleation or formation except for the presence of porosity. The heat affected zone and large grains are not relevant at the applied stress, and the spall damage still forms roughly where expected.

The combination of the experimental quasi-static and dynamic strength testing shows that the viability of using additive manufacturing to restore the performance of damaged components depends strongly on the intended use case of the repaired part in addition to the overall quality of the repair. Porous or contaminated repairs will likely be unacceptable in any use case. Clean repairs with full density but significant differences in the microstructure and ductility (as compared to the properties of the original part) may be acceptable under high strain-rate loading but not under quasi-static loading. The quantitative metric for acceptability may ultimately depend on the component and AM technique in question, but the results presented in this work emphasize that the strain rate in the intended loading case is a significant factor that must be considered when making that determination.

V. CONCLUSIONS

This work has presented an experimental investigation into the applicability of laser wire-fed additive manufacturing for repairing small-scale damage sites in 1100 aluminum. Tensile dogbones were intentionally and systematically scratched with a cutting tool and subsequently repaired using AM. Low strain-rate (10^{-3} s^{-1}) tests showed that the repaired samples were significantly weaker and less ductile overall. SEM imaging showed that the AM repair region was responsible for the lower ductility and changed the failure mode from very ductile to more brittle. Samples were also tested at high strain-rate (10^5 s^{-1}) using a light-gas gun to create incipient spall damage. The shock loading targets were damaged with either a scratch or an indent and repaired using the same AM process. The repaired samples showed very similar performance to the pristine cases at high strain-rate, provided the repair was fully dense. The un-repaired samples showed a dramatically different performance from the pristine case as expected, including geometric inversion of the indents but not the scratch damage sites. The *in situ* velocimetry and calculated spall strength as well as the qualitative post-mortem damage formation were all shown to be satisfactory or within margin of error for the repaired samples. This work has demonstrated the necessity for considering the strain-rate in addition to the maximum force of the anticipated loading case for parts that may be repaired with additive manufacturing. Future work investigating higher shock loading pressures may show that, like the quasi-static cases presented here, the AM repair performance can track the pristine sample to a point but beyond that

the repair fails and compromises the overall component. However, for the applied high strain-rate peak stress in this study (up to the incipient spallation point of the material), the AM repair appears promising.

ACKNOWLEDGMENTS

The authors acknowledge the support of the Los Alamos National Laboratory Directed Research and Development Program. This work was performed, in part, at the Center for Integrated Nanotechnologies, an Office of Science User Facility operated for the U.S. Department of Energy (DOE) Office of Science. Los Alamos National Laboratory, an affirmative action equal opportunity employer, is managed by Triad National Security, LLC for the U.S. Department of Energy's NNSA, under Contract No. 89233218CNA000001.

AUTHOR DECLARATIONS

Conflict of Interest

The authors have no conflicts to disclose.

Author Contributions

Jesse G. Callanan: Conceptualization (equal); Data curation (equal); Investigation (equal); Methodology (equal); Validation (equal); Visualization (equal); Writing – original draft (equal); Writing – review & editing (equal). **Daniel T. Martinez:** Data curation (equal); Investigation (equal); Methodology (equal). **Sara Ricci:** Data curation (supporting). **Nicholas K. Brewer:** Data curation (supporting). **Benjamin K. Derby:** Data curation (supporting). **Brandon J. Lovato:** Data curation (supporting). **Kendall J. Hollis:** Funding acquisition (equal); Project administration (equal). **Saryu J. Fensin:** Funding acquisition (equal); Project administration (equal); Supervision (equal). **David R. Jones:** Conceptualization (equal); Data curation (equal); Funding acquisition (equal); Investigation (equal); Methodology (equal); Project administration (equal); Supervision (equal); Validation (equal).

DATA AVAILABILITY

The data that support the findings of this study are available from the corresponding author upon reasonable request.

REFERENCES

- ¹K. Derekar, “A review of wire arc additive manufacturing and advances in wire arc additive manufacturing of aluminium,” *Mater. Sci. Technol.* **34**, 895–916 (2018).
- ²A. Aversa, G. Marchese, A. Saboori, E. Bassini, D. Manfredi, S. Biamino, D. Ugués, P. Fino, and M. Lombardi, “New aluminum alloys specifically designed for laser powder bed fusion: A review,” *Materials* **12**, 1007 (2019).
- ³Z. Zhu, Z. Hu, H. L. Seet, T. Liu, W. Liao, U. Ramamurthy, and S. M. L. Nai, “Recent progress on the additive manufacturing of aluminum alloys and aluminum matrix composites: Microstructure, properties, and applications,” *Inter. J. Machine Tools Manufact.* **190**, 104047 (2023).
- ⁴G. Langelandsvik, O. M. Akselsen, T. Furu, and H. J. Roven, “Review of aluminum alloy development for wire arc additive manufacturing,” *Materials* **14**, 5370 (2021).

- ⁵S. Dixit and S. Liu, "Laser additive manufacturing of high-strength aluminum alloys: Challenges and strategies," *J. Manufact. Mater. Process.* **6**, 156 (2022).
- ⁶P. A. Rometsch, Y. Zhu, X. Wu, and A. Huang, "Review of high-strength aluminum alloys for additive manufacturing by laser powder bed fusion," *Mater. Des.* **219**, 110779 (2022).
- ⁷M. Köhler, S. Fiebig, J. Hensel, and K. Dilger, "Wire and arc additive manufacturing of aluminum components," *Metals* **9**, 608 (2019).
- ⁸X. Guo, H. Li, P. Xue, Z. Pan, R. Xu, D. Ni, and Z. Ma, "Microstructure and mechanical properties of 600 mpa grade ultra-high strength aluminum alloy fabricated by wire-arc additive manufacturing," *J. Mater. Sci. Technol.* **149**, 56–66 (2023).
- ⁹Y. Ding, J. Muñoz-Lerma, M. Trask, S. Chou, A. Walker, and M. Brochu, "Microstructure and mechanical property considerations in additive manufacturing of aluminum alloys," *MRS Bull.* **41**, 745–751 (2016).
- ¹⁰T. Klein and M. Schnall, "Control of macro-/microstructure and mechanical properties of a wire-arc additive manufactured aluminum alloy," *Inter. J. Adv. Manuf. Technol.* **108**, 235–244 (2020).
- ¹¹J. G. Callanan, A. N. Black, S. K. Lawrence, D. R. Jones, D. T. Martinez, R. M. Martinez, and S. J. Fensin, "Dynamic properties of 316L stainless steel repaired using electron beam additive manufacturing," *Acta. Mater.* **246**, 118636 (2023).
- ¹²J. G. Callanan, D. T. Martinez, S. Ricci, B. K. Derby, K. J. Hollis, S. J. Fensin, and D. R. Jones, "Spall strength of additively repaired 304L stainless steel," *J. Appl. Phys.* **134**, 245102 (2023).
- ¹³X. Fang, G. Chen, J. Yang, Y. Xie, K. Huang, and B. Lu, "Wire and arc additive manufacturing of high-strength Al–Zn–Mg aluminum alloy," *Front. Mater.* **8**, 656429 (2021).
- ¹⁴D. Dolan, "Accuracy and precision in photonic Doppler velocimetry," *Rev. Sci. Instrum.* **81**, 053905 (2010).
- ¹⁵D. R. Jones, S. J. Fensin, O. Dippo, R. A. Beal, V. Livescu, D. T. Martinez, C. P. Trujillo, J. Florando, M. Kumar, and G. Gray, "Spall fracture in additive manufactured Ti-6Al-4V," *J. Appl. Phys.* **120**, 135902 (2016).
- ¹⁶G. Gray, *Shock Wave Testing of Ductile Materials* (ASM International, Materials Park, OH, 2000), pp. 530–538.
- ¹⁷T. Antoun, *Spall Fracture* (Springer Science & Business Media, 2003).
- ¹⁸S. P. Marsh, *LASL Shock Hugoniot Data* (University of California Press, 1980), Vol. 5.